ADVANCED MATERIALS
www.advmat.de

Ultra-Stretchable and Fast Self-Healing Ionic Hydrogel in Cryogenic Environments for Artificial Nerve Fiber

*Chan Wang, Ying Liu, Xuecheng Qu, Bojing Shi, Qiang Zheng, Xubo Lin, Shengyu Chao, Changyong Wang, Jin Zhou, Yu Sun, Gengsheng Mao, and Zhou Li**

Self-healing materials behave with irreplaceable advantages in biomimetic intelligent robots (BIR) for avoiding or reducing safety hazards and economic losses from accidental damage during service. However, the self-healing ability is unreservedly lost and even becomes rigid and fragile in the cryogenic environment where BIR are precisely needed. Here, the authors report a versatile ionic hydrogel with fast self-healing ability, ultra-stretchability, and stable conductivity, even at –80 °C. The hydrogel is systematically optimized to improve a hydrogen-bonded network nanostructure, coordinated achieving a quick self-healing ability within 10 min, large deformation tolerance of over 7000%, superior conductivity of 11.76 S cm^{-1} and anti-freezing ability, which is difficult to obtain simultaneously. Such a hydrogel provides new opportunities for artificial electronic devices in harsh environments. As a prospective application, they fabricate an artificial nerve fiber by mimicking the structure and functions of the myelinated axon, exhibiting the property of fast and potential-gated signal transmission. This artificial nerve fiber is integrated into a robot for demonstrating a real-time high fidelity and high throughput information interaction under big deformation and cryogenic temperature. The hydrogel and bionic device will bring pioneering functions for robots and open a broad application scenario in extreme conditions.

1. Introduction

Flexible and stretchable electronic devices are receiving risen attention in the fields of artificial skins,[1–3] soft robots,[4] and actuators for their compliance akin to that of biological systems.[5] The tissue-like modulus (kilopascal to gigapascal)[4,6,7] enables the deformable electronics to adapt to the complex interface of the human body or surroundings, but also be susceptible to accidental mechanical damages (puncture, scratches, and tear), which are the leading causes of device failure.[8] Developing self-healing materials can recover their morphology and functions in unexpected damages, which largely enhances the devices' service life, usage safety, and economic benefit. Numerous self-healing materials based on physical interdiffusion,[9] cardiovascular[8,10] or encapsulated healing agents,[11,12] dynamic covalent bonds[13–15] or non-covalent bonds,[4,16,17] and van der Waals forces[18] have been designed and successfully integrated

C. Wang, Y. Liu, X. Qu, B. Shi, Q. Zheng, S. Chao, Z. Li
CAS Center for Excellence in Nanoscience
Beijing Key Laboratory of Micro-Nano Energy and Sensor
Beijing Institute of Nanoenergy and Nanosystems
Chinese Academy of Sciences
Beijing 101400, China
E-mail: zli@binn.cas.cn

C. Wang, Y. Liu, X. Qu, S. Chao, Z. Li
School of Nanoscience and Technology
University of Chinese Academy of Sciences
Beijing 101400, China

B. Shi, X. Lin
Beijing Advanced Innovation Centre for Biomedical Engineering
Key Laboratory for Biomechanics and Mechanobiology of Ministry of Education
School of Biological Science and Medical Engineering
Beihang University
Beijing 100083, China

The ORCID identification number(s) for the author(s) of this article can be found under https://doi.org/10.1002/adma.202105416.

DOI: 10.1002/adma.202105416

Q. Zheng
School of Biology and Engineering
Guizhou Medical University
Guiyang 550025, China

C. Wang, J. Zhou
Beijing Institute of Basic Medical Sciences
Beijing 100850, China

Y. Sun, G. Mao
Department of Neurovascular Surgery
The Third Medical Centre Chinese People's Liberation Army General Hospital
Beijing 100036, China

Z. Li
Center on Nanoenergy Research
School of Physical Science and Technology
Guangxi University
Nanning 530004, China

Z. Li
Institute for Stem Cell and Regeneration
Chinese Academy of Sciences
Beijing 100101, China

into functional devices, such as epidermal sensors,[13,19] flexible touch screen,[2] and wearable energy generator. However, despite their promise, these self-healing materials still have substantial shortcomings that limit their applications in cryogenic environments, like in winter and high-latitude areas. The temperature sensitively self-healing process becomes slow or be prohibited at cold conditions for the diffusion of polymer segments and reformation of the broken dynamic interactions are restricted.[1,6,15,20] Therefore, the soft and deformable polymeric system with a low glass transition temperature (T_g) and abundant effective sites for dynamic interactions are expected.

Here, we proposed a versatile ionic hydrogel equipped with rapid self-healing capability, ultra-stretchability, high conductivity, and transparency, for applications in cryogenic environments. In the ternary system, hydroxyl-rich polyvinyl alcohol (PVA) and amino-rich polyethyleneimine (PEI) build the polymeric skeleton based on hydrogen bonds and electrostatic interactions, while plenty of bound water embedded in the skeleton at the state of clusters surrounding Li^+ serve as "flesh and blood." The strong hydration of Li^+ (ΔG° (Li^+) = –467 kJ mol^{-1})[21] breaks the directional arrangement of hydrogen bonds at sub-zero temperature, which guarantees continuous active dynamic interactions reconstruction and polymer segments diffusion during a self-healing process. Superior to other synthetic self-healing materials which need external stimulation to assist healing or dysfunctions at sub-zero conditions, the multiskilled hydrogel provides a universal material platform for artificial electronic devices by giving steady self-healing performance allied with conductivity and ultra-stretchability at both normal and cryogenic environments. To illustrate potential applications, we designed an artificial nerve fiber through mimicking the myelinated axon's structure and functions of signal transmission. When integrated into a multifunctional robot, the artificial nerve fiber demonstrated their real-time high fidelity and high throughput information interaction under big deformation and cold conditions.

2. Ultra-Stretchable and Fast Self-Healing Ionic Hydrogel (SSIH)

To prepare ionic hydrogels that maintain self-healing and conductive capacities in frozen environments, we pre-evaluated the frost resistance of four types of colligative inorganic salt. The lithium chloride (LiCl, both in solution and gel) behaves with outstanding anti-freezing performance with no attenuation in transparency and modulus after quite a long time in –80 °C (Figure S1, Supporting Information). We previously reported a stretchable elastomer with adjustable modulus based on PVA and branched polyethyleneimine (b-PEI), that presents potential applications in epidermal electronics with biocompatibility and availability[22] (**Figure 1**a-i). With the introducing of LiCl, the ternary system acquired the capacities of anti-freezing and self-healing, and the stretchability was also greatly improved (Figure 1a-ii).

The autonomous healing property of the hydrogel could be optimized by enhancing polymer segments' mobility and increasing dynamic hydrogen bonds.[1,12] In the binary system of PVA and PEI, the electrostatic interactions (Figure S2, Supporting Information) and abundant intramolecular/intermolecular hydrogen bonds help build an elastic 3D network but also lead to crystalline regions and the polymer chain shrinks, which limits better ductility and causes brittle fracture during stretching.[22,23] After the joint of LiCl, the ternary system's crystallinity greatly decreased and gradually transformed into a uniform single-phase (Figure S3, Supporting Information).[24] The strong hydration of Li^+ helps to transform free water into the bound state, break the directional alignment of hydrogen bonds in crystalline regions, and further release the locked hydrogen bonds into active states that could participate in breaking and reforming. According to the proton nuclear magnetic resonance (H^1 NMR), the peaks positioned between 3.5 and 4.0 ppm represent the proton of water in the hydrogel. (Figure S4, Supporting Information). With the increase of Li^+ content, peaks of protons in water shift to the low field and broaden, indicating that more dynamic hydrogen bonds are formed.[25] Similarly, X-ray photoelectron spectroscopy (XPS) demonstrates more $-OH$ from free water and PVA as well as $-NH_2$ from b-PEI are participating in forming dynamic hydrogen bonds[26] (Figure S5, Supporting Information). In addition, the joint of LiCl reduces the T_g through promoting the polymer segments' mobility of the system, which is crucial for the rapid diffusion of polymer segments during the healing process.[27] From dynamic mechanical analysis (DMA), the T_g of SSIH with 25% LiCl was found at –71.55 °C (Figure S6, Supporting Information).[28] Figure 1a,b gives a clear schematic illustration of SSIH's design process, the principle of self-healing capacity and ultra-stretchability.

The intrinsic performance of SSIH about frost resistance, stretchability, conductivity, and self-healing capacity could be coordination optimized by tuning the content of LiCl. Firstly, as the basis requirement for applying in cryogenic environments,[29] frost resistance was evaluated by the remaining participants at –80 °C and observing their morphology changes. The hydrogel with 25% content LiCl kept the original transparency and stretchability, while the sample without LiCl was frozen completely, being brittle and easily broken under slight strain (Figure 1c). That mainly credits to the strong hydration of Li^+ inhibiting the directional arrangement of water molecules (Figure S7, Supporting Information). Second, the addition of LiCl significantly optimizes the mechanical stretchability and performance stability. On the one hand, hard crystalline regions' reduction enables the hydrogel to afford larger deformation without fracture. On the other hand, more dynamic hydrogen bonds released from the crystalline area dissipate larger energy and homogenize the network through breaking and rebuilding during load applied cycles. Figure 1d and Figure S8, Supporting Information, show the SSIH exhibited higher strain failure points and lower maximum tensile stress as the LiCl content increases from 0% to 25%. The SSIH with 25% LiCl content could be surprisingly stretched to 70.46 times to its original length at a loading rate of 30 mm min^{-1}, which is ≈23.9 folds to the sample without LiCl. The strong hydration of Li^+ also brings the ionic hydrogel an excellent water retention capacity and mechanical performance stability. After 12 months, the SSIH with 25% LiCl kept 92% water content compared to the original state, and the max tensile deformation remained 4940% deformation (Figure S9, Supporting Information). Furthermore, the intrinsic conductivity of the ionic

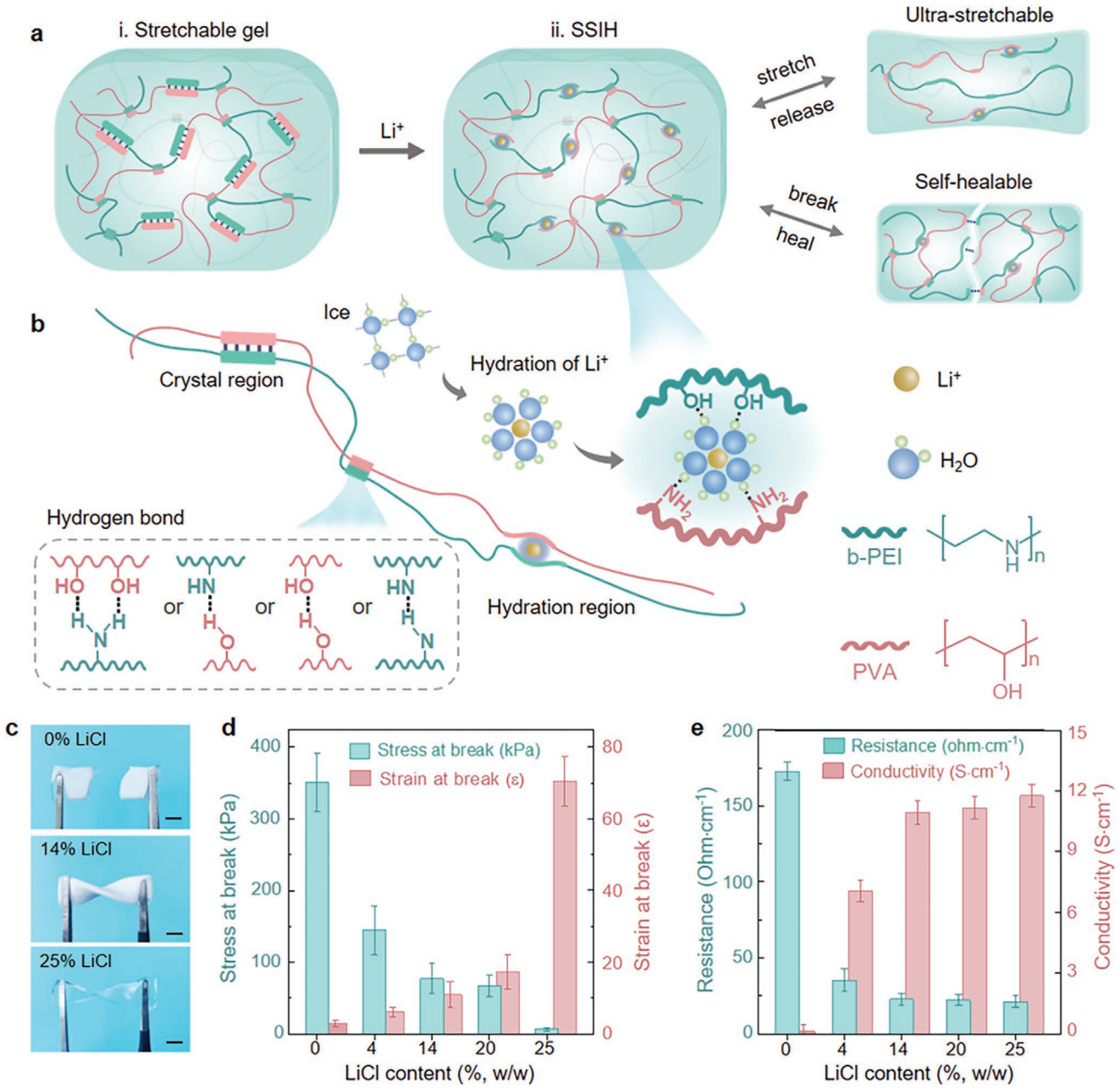

Figure 1. The design principle of SSIH for the cryogenic environment. a) The design process of SSIH and the principle of self-healing ability and ultra-stretchability. b) Interactions in SSIH contribute to the self-healing process. c) With the increase of LiCl, the anti-freezing ability and flexibility of SSIH grew better. Scale bar: 0.5 cm. d) As the LiCl content increases, the elongation at break of SSIH increases to ≈70 times to original length. On the contrary, the tensile strength decreased. e) Along with the increase of LiCl, the conductivity of SSIH showed a growth trend.

hydrogel was enhanced to11.76 S cm^{-1} as LiCl content increased to 25% (Figure 1e) for more free ions participating in conduction.[30] Thus, the optimal SSIH with 25% LiCl (abbreviated as SSIH in the following) was selected for further study.

2.1. Self-Healing Properties of SSIH

To deep understand the autonomous self-healing behavior, extreme mechanical damage was created by separating SSIH completely into two pieces and observing the healing process after bringing the damaged hydrogel together slightly. Based on the reversible interactions, the structure-network and functions recovered quickly (**Figure 2**a). The molecular dynamics (MD) simulation verified the feasibility of the self-healing mechanism (Figure S10, Supporting Information).[31] Intuitionally, the healing process at the damaged surface was observed, where the notch grew together after 5 min healing and entirely disappeared within 10 min at room temperature (Figure 2b). Except for repairing one damaged sample, the SSIH fabricated

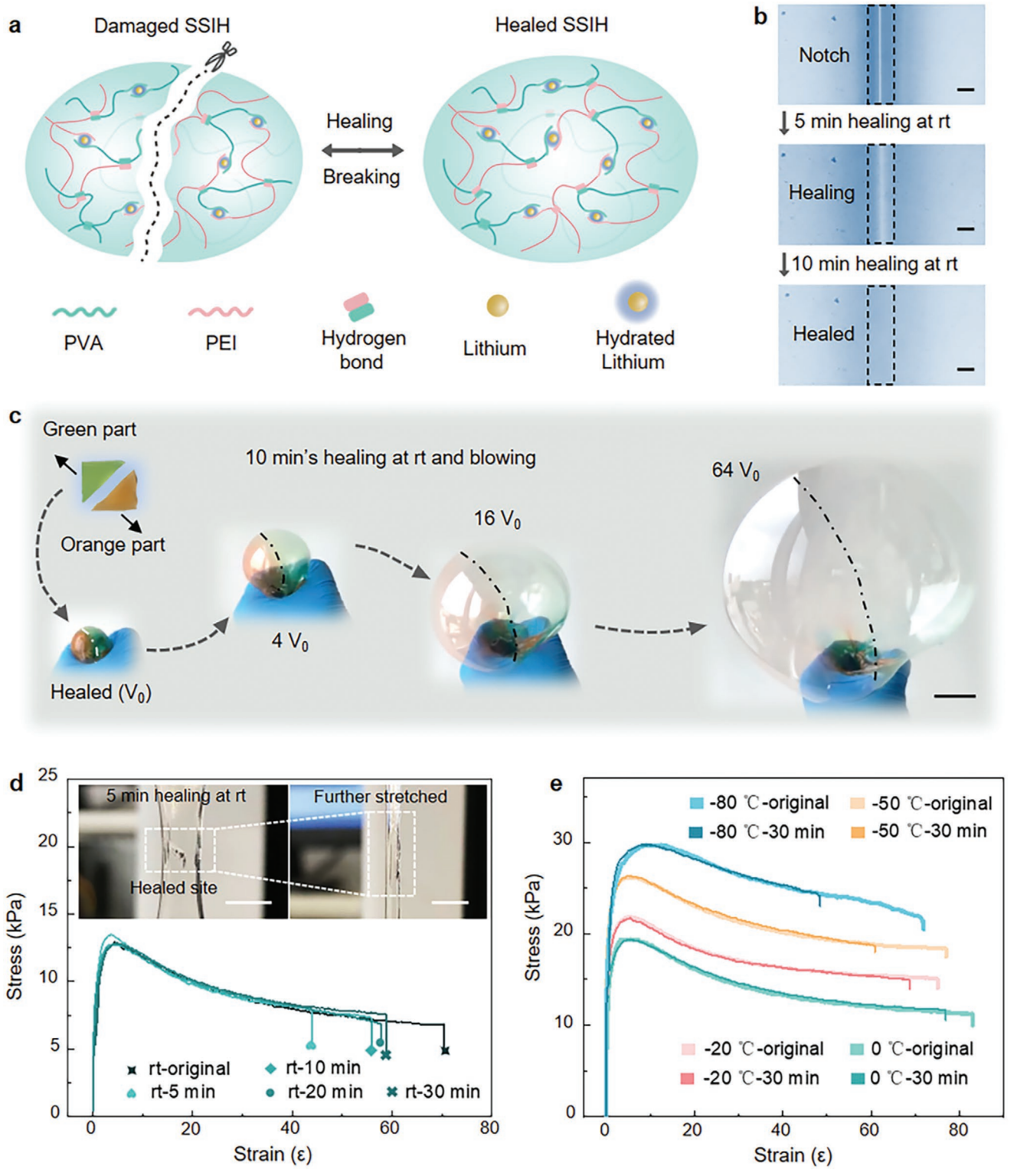

Figure 2. Self-healing mechanism and properties of SSIH. a) The self-healing mechanism of SSIH. b) The self-healing process of one damaged SSIH was observed through the optical microscope. Scale bar: 2 mm. c) The self-healing performance of two SSIHs. Scale bar: 2 cm. d) The tensile stress–strain curves of SSIH at the original state and different healing times at room temperature. The insets show notch of SSIH at stretched states after 5 min healing. Scale bar: 1 cm. e) The tensile stress–strain curves of SSIHs at the original state and after 30 min healing in cryogenic temperatures. The original size of all samples: $10 \times 10 \times 1$ mm^3. Loading rate: 30 mm min^{-1}.

at different time achieved same healing effect by attaching together slightly. For better visualization, two SSIHs were dyed into green and orange, respectively. After 10 min, the SSIHs grew together thoroughly but with clear boundary, indicating the healing process does not change polymer network conformation. Pumping air, even the healed sample was expanded to 64 times to original volume, no gas leaked out (Figure 2c). In the same way, colorful SSIHs were assembled into multiple shapes and structures, like a rocket, tree, and fish (Figure S11, Supporting Information). The scalability of the SSIH simplifies the device preparation process and avoids adhesives, which is of great significance for large-scale integrated systems.

Healing efficiency, defined as the proportion of fracture energy restored relative to that of the original state, is a significant parameter to quantify the mechanical properties recovery.[16] For all samples in Figure 2d,e, and Figure S12, Supporting Information, the SSIHs maintained their Young's modulus and showed the similar tensile stress–strain curves. It's the elastic deformation at the beginning part of tensile loading and plastic deformation after yield point, which illustrates the healing process and lower ambient temperature made a slight impact on the conformation and properties of the hydrogel. At 30 °C, the hydrogel recovered ≈69.46% in 5 min and elevated to 84.31% after 10 min healing with 5586% deformation (Figure 2d and Figure S13, Supporting Information).

Decreasing temperature, the self-healing ability of SSIHs well maintained, ≈92.96%, ≈92.0%, ≈82.11%, and ≈71.57% recovery efficiency achieved after 30 min healing at 0, −20, −50, and −80 °C (Figure 2e), respectively. For frozen environments, such as −80 °C, the healing process slightly slowed down due to the restricted polymer segments diffusion and dynamic interactions reorganization, and then self-healing efficiency could be improved by extending the healing time. The healing efficiency of all samples is calculated and summarized in Figure S14, Supporting Information. Such reduced healing temperature and superior healing efficiency within a brief period position the SSIH in a previously unexplored area of anti-freezing and self-healing materials (Figure S15 and Table S1, Supporting Information) and broaden their application scenes in extreme environments.

2.2. Electrical Properties of SSIH

We have demonstrated that more LiCl elevated conductivity and then screened the SSIH (11.76 S cm^{-1}, Figure S16, Supporting Information) to explore the effect of temperature on conductance. The electrochemical impedance spectra (EIS) show a temperature-related impedance. (**Figure 3**a–c and Figure S17, Supporting Information). The equivalent resistance (ER)[32] of SSIH increased moderately for every 10 °C from 30 to −80 °C (Figure 3d) for colder environment limited ions' mobility and brought conductance bereft. The stable electrical performance of SSIH at −80 °C dramatically extended the application temperature range compared to other conductive materials (Figure S15, Supporting Information). Furthermore, after 13 months of refrigerating at −80 °C, the resistance of SSIH increased slightly and stayed at 440.9 ohm cm^{-1}, indicating long-term stability (Figure 3e and Figure S18, Supporting Information). The electrical healing ability of SSIH in cryogenic environments was also demonstrated through healing evaluation after cutting SSIH into two parts. As it was touched, the red LED recovered brightness at once. After 30 min healing without external stimuli and additional substance supplement, the healed sample sustained 200% deformation without rupture (Figure 3f and Movie S1, Supporting Information).

Electrical signal transmission with high-frequency and low-intensity carries more information but consumes less energy. Then, we investigated the SSIH's impedance response to frequency and voltage at sub-zero temperature. The impedance plot (Figure 3g) performed a relatively reposeful region from 10^4 to 10^5 Hz at 30 °C. At lower temperatures, the resistance of SSIH increases and behaves with a tendency of enlarging stable area range and moving towards a small frequency. When the temperature was reduced to −80 °C, the resistance increased to 66.4 kOhm and kept relatively constant from 10^1 to 10^4 Hz, providing a large operating window. A similar trend could be found in the phase plot, the frequency range of phase angle close to 0° shift to the smaller frequency along with temperature decreased (Figure 3h). Surprisingly, the colder environments also broaden the working voltage window of SSIH (Figure S19, Supporting Information). The inflection points of the current curves caused by the electrolysis of water in the system transferred from 1.0 (30 °C) to 1.98 V (−80 °C), for more water molecules were bound between the PVA or PEI segments and around Li^+ in state of combined and hydrated water. In conclusion, the high and stable conductivity, fast recovery after injury, enlarged frequency range with stable impedance, and large working voltage window make SSIH a strong candidate for stretchable artificial devices.

3. An Ultra-Stretchable and Self-Healing Artificial Nerve Fiber (SSANF)

The information transmission unit compatible with the flexible electronic system is essential in connecting functional parts. Organic conductive materials have been widely studied to overcome the hardness and brittleness of traditional metal wire. However, the stretchable conductor's intrinsic resistance and strain sensitivity also lead to large driving voltage, heat loss, and an unstable signal transmitting performance. In addition to improving the intrinsic conductivity through material performance optimization, the information transmission performance could be optimized through structural design.

The mammalian nervous system possesses multiple functions of sensing, acting, and high-throughput ionic information transmission, which is the most powerful ion circuit in nature. Once the ionic signal is generated, the ion-carried information will be quickly sent to the corresponding organs and tissues. The myelinated axons plays big roles in this procedure with the unique structure, where the saline solution wrapped by insulating myelin sheath forms a capacitance model for fast nerve impulse transferring (**Figure 4**a-i).[33,34] Inspired by the myelinated axons' structure and function of action potential delivery, a potential-gated artificial nerve fiber with properties of being ultra-stretchable and self-healing for high-throughput and fast ionic information transmission was designed. Two

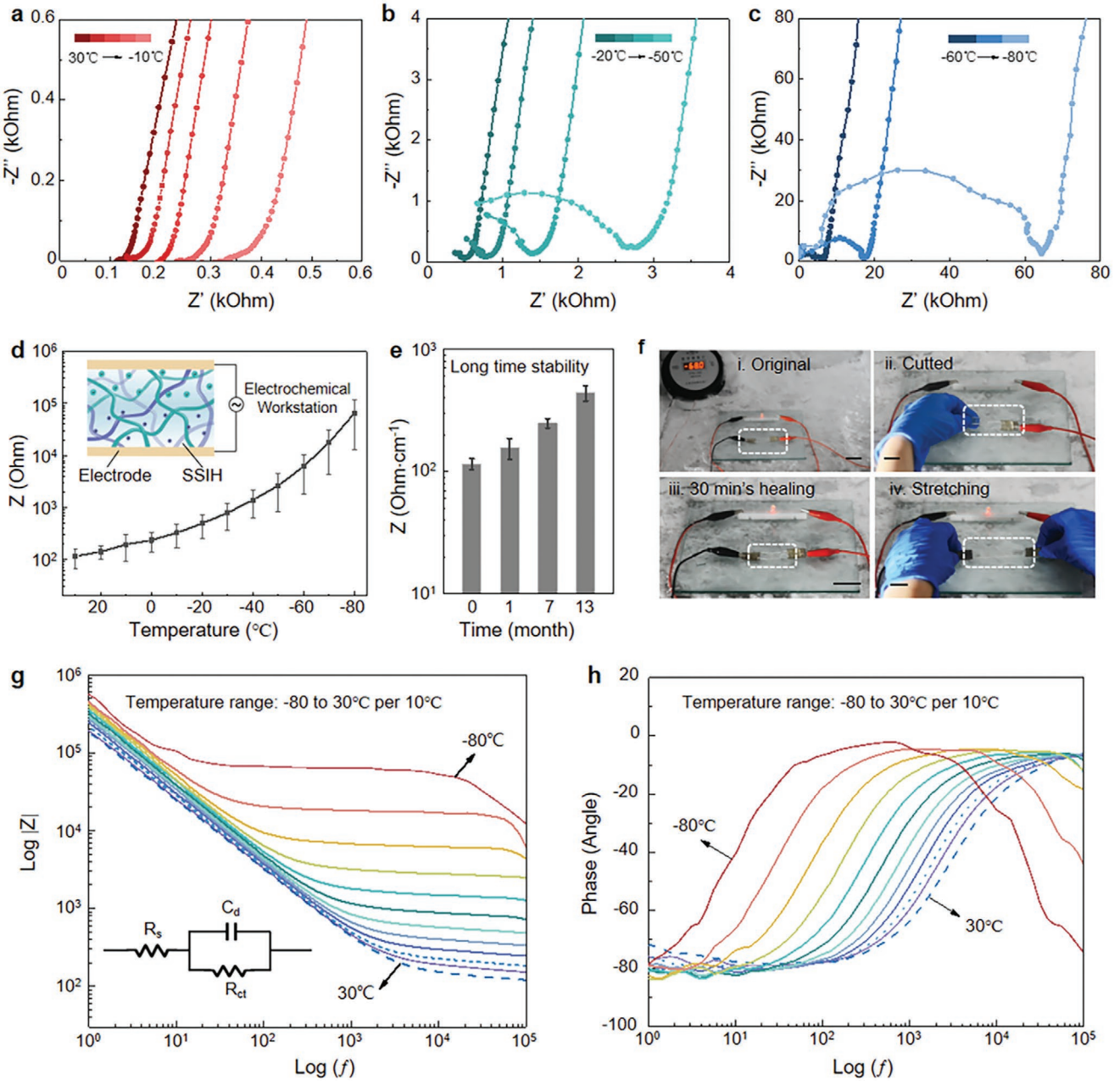

Figure 3. Electrical properties of SSIH. a–c) The EIS plot of SSIH from 30 to −80 °C with temperature decreased per 10 °C. All samples' size: 10 × 10 × 2 mm^3. d) The resistance of SSIH increased with temperature reduced. The inset schematic displays ions' responses during tests. e) The hydrogel exhibited enduring conductive stability, and the resistance just increased to 440.9 ohm cm^{-1} after 13 months, kept in the air at −80 °C. f) The electrical self-healing capacity of SSIH at −68 °C. g) The reposeful platform of impedance expanded and moved to lower frequency as the temperature decreased. The inset shows the Equivalent circuit. h) The platform of phase angle close to 0° shifted to lower frequency along with temperature decreased.

parallel stripped SSIHs, mimicking the cytosol as the electrolyte, are separated by a dielectric elastomer which imitated a myelin sheath (Figure 4a-ii). With titanium foils as electrodes, one end of SSANF serves as input ports, connecting to the external signal source. The other end serves as output ports, connecting to the functional device.[34] When a time-depended voltage signal ($\approx V_0$) is applied at the input port, the electrode and ionic hydrogel interface forms an electrical double layer (EDL). Then the EDL transmits along with the device to the output ports ($\approx V_1$) (Figure 4a-ii). To evaluate SSANF's information transmitting performance, we used the signal generator as an input signal source and an oscilloscope to display the curves before and after transmission (inset of Figure 4c). There were almost no phase and shape changes of V_1 compared with V_0 when the frequency varied from 1 Hz to 1 MHz, and the voltage amplitude varied from 100 mV to 20 V (Figure 4b and Figure S20, Supporting Information). Accurately, the value of $|V_1/V_0|$ kept between 0.975 and 1.025, indicating the good information

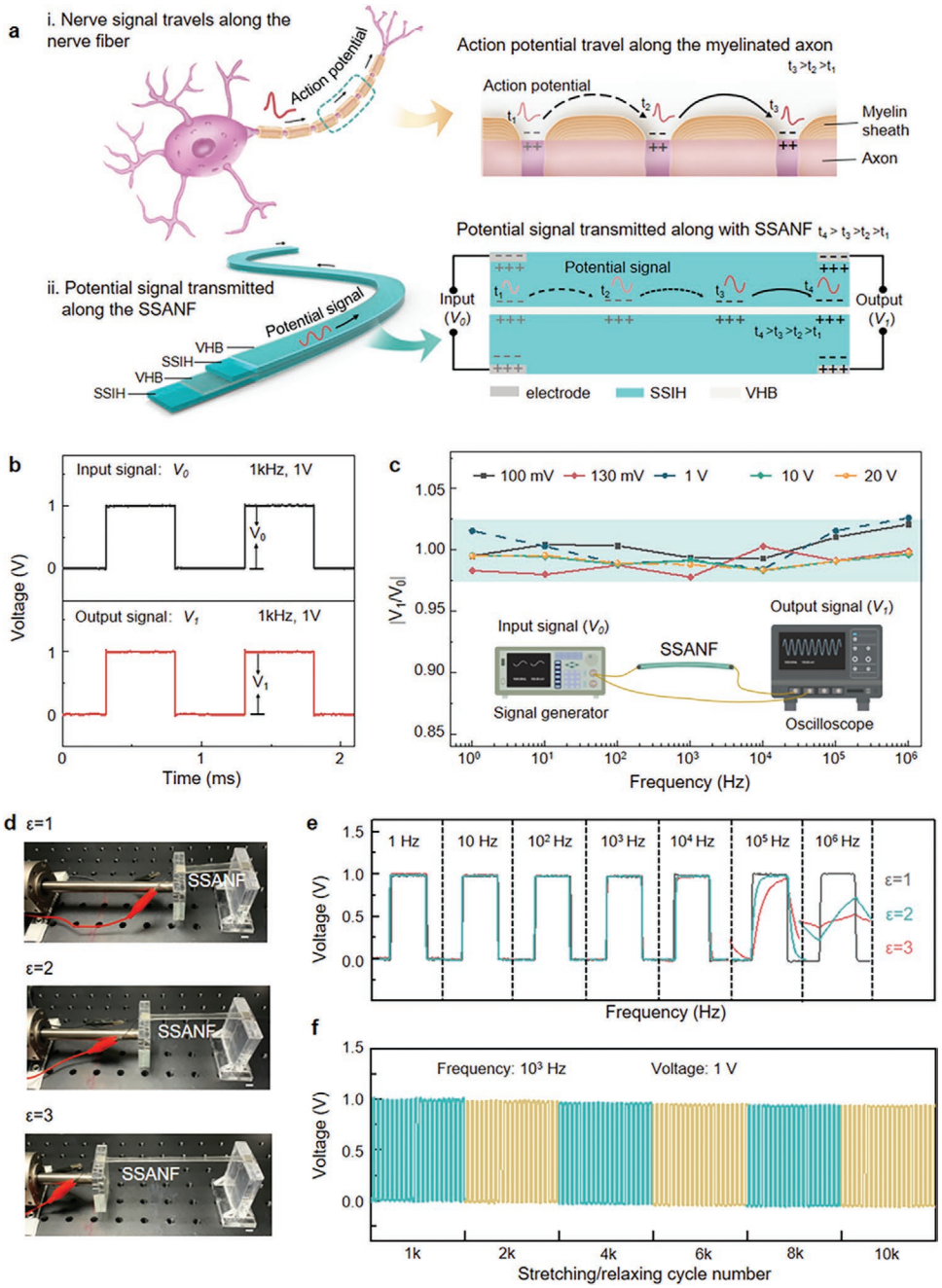

Figure 4. Design principle and information transmission capacity of SSANF. a) Design principle of SSANF. i) Diagram about the myelinated axon's structure. The neural signal travels along the myelinated axon in the form of the action potential. ii) Diagram about the SSANF's structure. The potential signal transmitting process in a capacitance model. b) The signal transmitted by SSANF is well maintained in shape and amplitude. c) $|V_1/V_0|$ varied with frequency and amplitude of voltage pulses and kept value between 0.975 and 1.025. Inset shows the test equipment. Under 100%, 200%, and 300% deformation (d), signal curves recorded in output port (e). f) During 10 000 times of stretching to 200% deformation and releasing, the signal kept its initial shape and amplitude.

transmission fidelity of SSANF (Figure 4c). The performance stability of SSANF with a tensile deformation of 100%, 200%, and 300% were tested (Figure 4d,e). The V_1 kept synchronous curves with V_0, slight phase delay and shape changes appeared, which were mainly ascribed to the longer transfer distance under larger deformation. Under 200% deformation, SSANF behaved with good fatigue resistance during 10 000 times stretching and releasing cycles (Figure 4f). In addition, SSANF also demonstrated high fidelity transmission for other voltage signals, such as triangular wave and sine wave in different amplitudes (Figure S21, Supporting Information).

Taking advantages of faithful and high throughput information interaction and long-term working stability, the SSANF is expected to work as a communication unit for message and

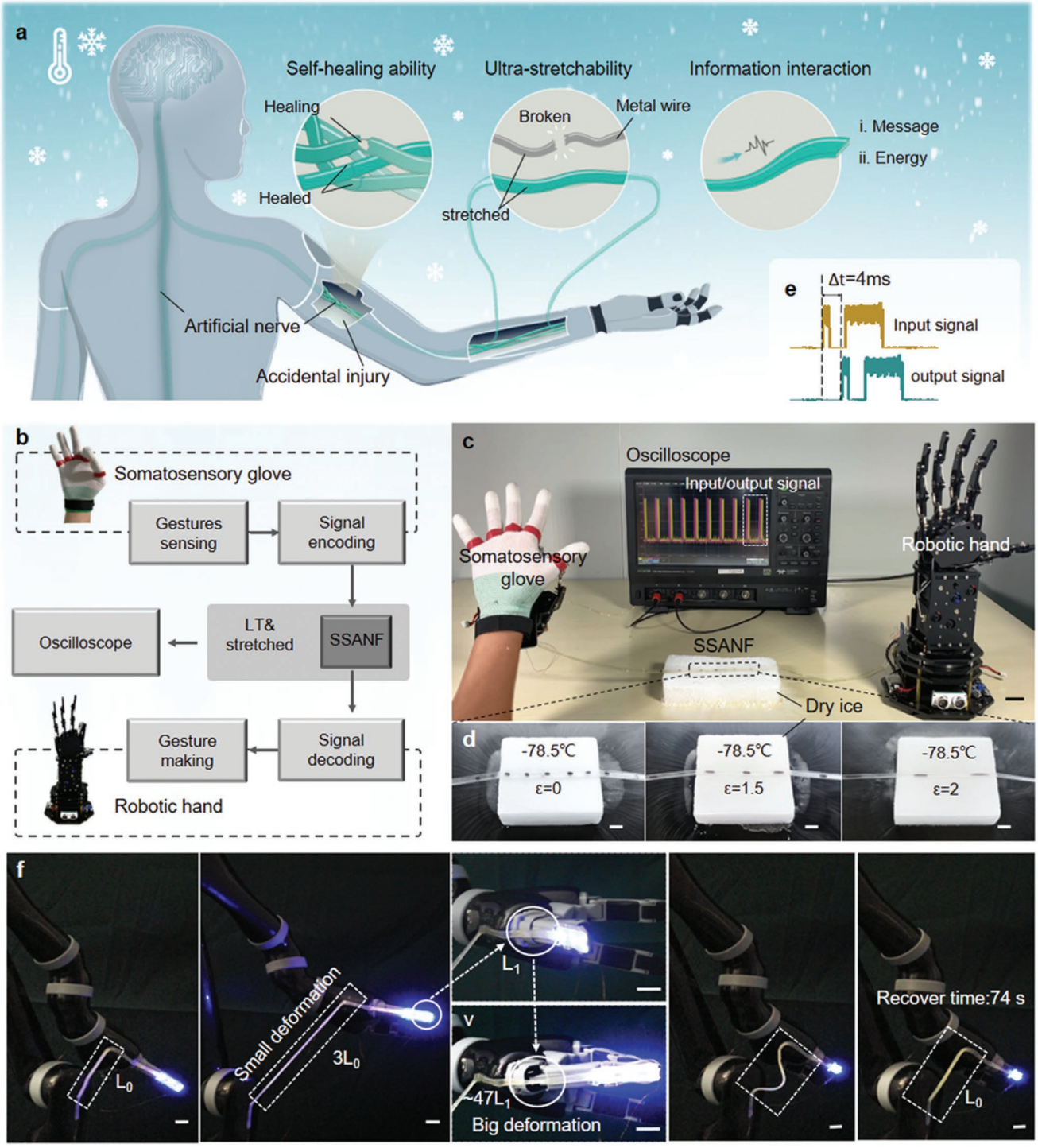

Figure 5. Application of SSANF in biomimetic intelligent robots (BIR). a) SSANF is expected to work as a communication unit of BIR. The information interaction of SSANF helps transfer energy and message to the next part. b) Simple circuit diagram of synchronous bionic robotic hand system, c) where SSANF was used to transmit real-time integrated signals. d) A local cryogenic environment was created by dry ice (–78.5 °C). Scale bar: 2 cm. e) The input and output signals of SSANF under 200% deformation and at –78.5 °C. Scale bar: 1 cm. f) Energy delivery ability and fast recovery of SSANF. Scale bar: 3 cm.

energy delivery. SSANF makes it possible to develop a transmutable and self-healable biomimetic intelligent robot (BIR) that could operate in extremely cold environments, like polar regions or outer space (**Figure 5**a). For potential applications in BIR, we evaluated the information transmission and energy delivery performance of SSANF, respectively. For real-time

message transmission of integrated signals, we equipped SSANF into a synchronous bionic robotic hand system, where the somatosensory glove connected to the input port of SSANF, the robotic hand linked to the output end, the oscilloscope connected at both ends (Figure 5b,c). Meanwhile, to create a cryogenic environment, a part of SSANF marked with black dots was fixed on the surface of dry ice (–78.5 °C) during the test (Figure 5d). After the somatosensory glove recognizing the hand movement (like Yeah, Ok, Good, and Rock) and encoding the gesture signals, SSANF transferred the integrated messages to the robotic hand to decode and make the same actions (Movie S2, Supporting Information). The incoming and outgoing signals were recorded by oscilloscope and displayed a time difference of ≈4 ms due to the length of SSANF (≈30 cm) (Figure 5e). Under 200% stretching/releasing cycles and –78.5 °C, the synchronous action of the robotic hand was not interrupted, indicating good transmission stability of SSANF. The SSANF was attached to a robotic arm with light-emitting diodes (LEDs) connected with the output port for energy delivery. Under the small deformation at the elbow and the large deformation at the joint during an extension action of the robotic arm, SSANF maintained stable energy delivery with slight attenuation of the LEDs' brightness. Besides, SSANF recovered to its original length within 74 s after deformation was released, which is essential for long-term work stability (Figure 5f and Movie S3, Supporting Information).

4. Conclusion

Aiming at two main factors that affect self-healing behavior in cryogenic environments, we proposed a facile and universal strategy to endow hydrogel self-healing ability through releasing "locked" active sites and increasing mobility of polymer segments. The as-fabricated ionic hydrogel achieved fast self-healing within 10 min, more than 7000% tensile deformation and superior conductivity of 11.76 S cm^{-1} at 30 °C. In particular, these practical properties were well-kept at freezing environments, even at –80 °C, which addressed current limitations in gel-based self-healing materials that disfunction at sub-zero temperatures due to the congelation of moistures and polymer segments.

With remarkable mechanical and electrical self-healing performance in cryogenic environments, the ionic hydrogel makes many research directions and applications possible by providing a universal material platform. In this work, we illustrated an artificial nerve fiber based on SSIH for high fidelity and high throughput information interaction by mimicking the myelinated axon's structure and function of signal transmission. The artificial nerve fiber demonstrated its use in real-time integrated signals delivery when linked into a multifunctional robot. Under repeating large deformation, the steady performance of SSANF overcomes the shortcomings of traditional metallic wires that are rigid and fragile, making it possible for fully flexible integrated systems. The gel-based bionic device will bring the BIR closer to simulating complex biological systems and open a broader application scenario for robots to complete unmanned missions in extreme conditions.

5. Experimental Section

Synthesis of SSIH: The SSIH was synthesized as following steps. Briefly, the homogeneous solution was prepared by dissolving 2.0 g PVA power (PVA, CAS: 9002-89-5,1799, MW = 89 000–98 000, 99%, E1921191), 1.0 g PEI (PEI, CAS: 9002-98-6, MW = 600, 99%, E1927073), and 4.0 g LiCl (LiCl, CAS: 7447-41-8, MW = 42.39, AR 99%, C10433364) in 9.0 mL deionized water and then heating in a water bath (98 °C) via magnetic stirring for 2 h. Then, the sol was shaped in a glass mold and cooled at –20 °C overnight. After thawed at room temperature for 12 h, they got SSIH for further study. Other samples with different LiCl content were prepared in the same procedures. More details can be found in Table S2, Supporting Information.

Fabrication of SSANF: SSANF was prepared in a sandwich structure with two parallel SSIHs (1 mm) interlining the dielectric elastomer (1 mm, 3M VHB 9469). Four pieces of titanium sheets were connected with the terminal part of SSIH (as stated in Figure 4a-ii) as electrodes. The titanium sheets need pre-cleaning to reduce contact resistance by polishing the surface oxide layer. A 0.2 mm VHB film deposited with 3 µm parylene-C was used as encapsulation. SSANFs used in Figure 4 and Figure 5 were designed into different dimension parameters according to experiment requirements.

Structure Characterization of SSIHs: X-ray diffraction (XRD) was performed using PANalytical X'Pert3 Power with 2θ ranged from 5° to 80°, where Cu Kα radiation (λ = 1.5406Å) were operated at 40 kV and 40 mA. X-ray photoelectron spectra (XPS) were recorded by PHI 5000 VersaProbe III with aluminum Kα source (1848.6 eV) and a collimator at 15 kV and 50 W. The high-resolution survey of nitrogen and oxygen was performed with pass energy = 69 eV. Proton nuclear magnetic resonance (1H NMR) spectra were recorded on a Bruker AVANCE III 700 MHz spectrometer with deuterated DMSO as solvent at room temperature. Dynamic mechanical analysis (DMA) was carried out under tension in the air atmosphere (Q800, TA Instruments) with samples dimension of $8.0 \times 8.2 \times 0.67$ mm^3. A tensile preload force of 0.01 N was applied and small oscillations of amplitude 1% strain were applied at 1 Hz frequency. A temperature sweep from –80 to 20 °C was performed with a rate of 5 °C min^{-1}.

Mechanical Self-Healing Properties of SSIH: Tensile experiments were performed by ESM301/Mark-10 system with a strain speed of 30 mm min^{-1}. All samples were shaped into sizes of $10 \times 10 \times 1$ mm^3. The polymer films were cut into two pieces for the self-healing tests and put together to heal after remained in different conditions for 2 h. Then tensile-stress tests of healed samples were executed following the same procedure. Optical photographs of the healed sites were exhibited by an optical microscope (Nikon ECLIPSE 3×2 STAGE JAPAN).

Electrical Self-Healing Properties of SSIH: The resistance of SSIH at different conductions was measured with CHI 660E electrochemical workstation. EIS spectra were obtained at a range of 1 MHz to 0.1 Hz with an AC amplitude of 10 mV. Local low-temperature environments in tests were created through Linkam cold platform (LTSE420). Resistance dates in Figure 3d were calculated from three samples with every sample test three times. For long time stability, the resistance of SSIH after remaining in a period (in –80 °C) was measured through EIS after placing it at room temperature for 4 h. For electrical self-healing tests, after being kept in a –80 °C refrigerator for 2 h, the rectangular shape sample size of $30 \times 10 \times 2$ mm^3 was scissored in half and brought together gently. The decomposition potential of samples was measured by Semiconductor Characterization System (Keithley 4200A-SCS).

Information Transmission of SSANF: For signal transmission performance of SSANF, a signal generator (RIGOL, DG4062) linked with the input port of SSANF was used to produce voltage pulse with frequency from 1 Hz to 1 MHz and amplitude range from 90 mV to 20 V. The input and output signals were displayed by an oscilloscope (LeCroy, HDO6104). Fatigue tests during 10 000 times stretching/releasing cycles were performed with SSANF's one end fixed, and the other end adhered to the linear motor (LinMot E1100). The SSANFs used in the signal transmission performance tests were all in size of $50 \times 10 \times 3.4$ mm^3.

SSANF as Communication Unit in a Multifunctional Robot System: SSANF was integrated into a synchronous bionic robotic hand

system (Zhongling Technology, Gihand) through linking between the somatosensory glove and robotic hand. The cryogenic environment was created by dry ice. For real-time energy delivery, SSANF was attached to a deformable robotic arm (Kinova, Jaco2) with luminescence LEDs connected with the output port. A power source with alternating voltage with an amplitude of 7.5 V was connected with the input port. The sizes of SSANFs used in the multifunctional robot system are all in sizes of $300 \times 10 \times 3.4$ mm^3.

Supporting Information

Supporting Information is available from the Wiley Online Library or from the author.

Acknowledgements

This work was supported by the National Natural Science Foundation of China (No. T2125003, 61875015, 82001982, 32101117), the Beijing Natural Science Foundation (JQ20038, L212010), and the Strategic Priority Research Program of the Chinese Academy of Sciences (XDA16021101). The experiment with the the somatosensory glove involving human subject has been performed with the full, informed consent of the volunteer.

Conflict of Interest

The authors declare no conflict of interest.

Author Contributions

C.W. and Y.L. contributed equally to this work. C.W., Y.L., and Z.L. conceived the project. C.W. and Y.L. carried out the SSIH's design and preparation. C.W. and Y.L. accomplished the SSIH's mechanical and self-healing properties characterization. X.L. did the MD simulations. C.W. and Y.L. fabricated the SSANF. C.W., X.Q., and B.S. tested the basic signal transmission performance. C.W., Y.L., X.Q., B.S., Q.Z., J.Z., C.Y.W., Y.S., and G.M. designed the demo of SSANF in the biomimetic intelligent robot. C.W., Y.L., and X.Q took and processed the experiment videos. C.W., Y.L., and Q.Z. arranged the figures of manuscript. C.W., Y.L., and Z.L. wrote the manuscript. All authors reviewed and commented on the manuscript.

Data Availability Statement

The data that support the findings of this study are available from the corresponding author upon reasonable request.

Keywords

anti-freezing, artificial nerve fibers, self-healing ionic hydrogels, ultra-stretchability

Received: July 14, 2021
Revised: January 15, 2022
Published online:

[1] J. Kang, J. B. H. Tok, Z. Bao, *Nat. Electron.* **2019**, *2*, 144.
[2] G. Gao, F. Yang, F. Zhou, J. He, W. Lu, P. Xiao, H. Yan, C. Pan, T. Chen, Z. L. Wang, *Adv. Mater.* **2020**, *32*, 2004290.
[3] a) H. Guo, Y. Han, W. Zhao, J. Yang, L. Zhang, *Nat. Commun.* **2020**, *11*, 2037; b) Y. Wang, X. Huang, X. Zhang, *Nat. Commun.* **2021**, *12*, 1291; c) B. Ying, R. Z. Chen, R. Zuo, J. Li, X. Liu, *Adv. Funct. Mater.* **2021**, *31*, 2104665.
[4] A. Pena-Francesch, H. Jung, M. C. Demirel, M. Sitti, *Nat. Mater.* **2020**, *19*, 1230.
[5] G. Ge, Y. Zhang, J. Shao, W. Wang, W. Si, W. Huang, X. Dong, *Adv. Funct. Mater.* **2018**, *28*, 1802576.
[6] D. L. Taylor, M. in Het Panhuis, *Adv. Mater.* **2016**, *28*, 9060.
[7] S. Chen, L. Sun, X. Zhou, Y. Guo, J. Song, S. Qian, Z. Liu, Q. Guan, E. M. Jeffries, W. Liu, Y. Wang, C. He, Z. You, *Nat. Commun.* **2020**, *11*, 1107.
[8] J. F. Patrick, M. J. Robb, N. R. Sottos, J. S. Moore, S. R. White, *Nature* **2016**, *540*, 363.
[9] X. Chen, M. A. Dam, K. Ono, A. Mal, H. Shen, S. R. Nutt, K. Sheran, F. Wudl, *Science* **2002**, *295*, 1698.
[10] K. S. Toohey, N. R. Sottos, J. A. Lewis, J. S. Moore, S. R. White, *Nat. Mater.* **2007**, *6*, 581.
[11] S. R. White, N. R. Sottos, P. H. Geubelle, J. S. Moore, M. R. Kessler, S. R. Sriram, E. N. Brown, S. Viswanathan, *Nature* **2001**, *409*, 794.
[12] S. Wang, M. W. Urban, *Nat. Rev. Mater.* **2020**, *5*, 562.
[13] a) D. Son, J. Kang, O. Vardoulis, Y. Kim, N. Matsuhisa, J. Y. Oh, J. W. F. To, J. Mun, T. Katsumata, Y. Liu, A. F. McGuire, M. Krason, F. Molina-Lopez, J. Ham, U. Kraft, Y. Lee, Y. Yun, J. B. H. Tok, Z. Bao, *Nat. Nanotechnol.* **2018**, *13*, 1057.
[14] a) C.-H. Li, C. Wang, C. Keplinger, J.-L. Zuo, L. Jin, Y. Sun, P. Zheng, Y. Cao, F. Lissel, C. Linder, X.-Z. You, Z. Bao, *Nat. Chem.* **2016**, *8*, 618; b) T. S. Wong, S. H. Kang, S. K. Tang, E. J. Smythe, B. D. Hatton, A. Grinthal, J. Aizenberg, *Nature* **2011**, *477*, 443; c) Z. Liu, L. Zhang, Q. Guan, Y. Guo, J. Lou, D. Lei, S. Wang, S. Chen, L. Sun, H. Xuan, E. M. Jeffries, C. He, F.-L. Qing, Z. You, *Adv. Funct. Mater.* **2019**, *29*, 1901058.
[15] B. K. Ahn, D. W. Lee, J. N. Israelachvili, J. H. Waite, *Nat. Mater.* **2014**, *13*, 867.
[16] Y. Cao, Y. J. Tan, S. Li, W. W. Lee, H. Guo, Y. Cai, C. Wang, B. C. K. Tee, *Nat. Electron.* **2019**, *2*, 75.
[17] Z. Y. Lei, P. Y. Wu, *Nat. Commun.* **2018**, *9*, 75.
[18] D. Davydovich, M. W. Urban, *Nat. Commun.* **2020**, *11*, 5743.
[19] M. Wang, Z. Lai, X. Jin, T. Sun, H. Liu, H. Qi, *Adv. Funct. Mater.* **2021**, *31*, 2101957.
[20] a) Y. Xu, Q. Rong, T. Zhao, M. Liu, *Giant* **2020**, *2*, 100014; b) S. Xue, Y. Wu, M. Guo, Y. Xia, D. Liu, H. Zhou, W. Lei, *Soft Matter* **2019**, *15*, 3680; c) E. Filippidi, T. R. Cristiani, C. D. Eisenbach, J. H. Waite, J. N. Israelachvili, B. K. Ahn, M. T. Valentine, *Science* **2017**, *358*, 502.
[21] R. Puchta, M. Galle, N. E. Hommes, E. Pasgreta, R. Eldik, *Inorg. Chem.* **2004**, *43*, 8227.
[22] C. Wang, K. Hu, C. Zhao, Y. Zou, Y. Liu, X. Qu, D. Jiang, Z. Li, M. R. Zhang, Z. Li, *Small* **2020**, *16*, 1904758.
[23] a) T. Xia, M. Kovochich, M. Liong, H. Meng, S. Kabehie, S. George, J. I. Zink, A. E. Nel, *ACS Nano* **2009**, *3*, 3273; b) S. K. Burley, G. A. Petsko, *Adv. Protein Chem.* **1988**, *39*, 125.
[24] H. L. Abd El-Mohdy, *J. Polym. Res.* **2013**, *20*, 177.
[25] a) L. Zhang, Z. Liu, X. Wu, Q. Guan, S. Chen, L. Sun, Y. Guo, S. Wang, J. Song, E. M. Jeffries, C. He, F. L. Qing, X. Bao, Z. You, *Adv. Mater.* **2019**, 1901402; b) H. E. Gottlieb, V. Kotlyar, A. Nudelman, *J. Org. Chem.* **1997**, *62*, 7512.
[26] C. S. Fadley, *J. Electron Spectrosc. Relat. Phenom.* **2010**, *178*, 2.
[27] A. Ito, P. Phulkerd, V. Ayerdurai, M. Soga, A. Courtoux, A. Miyagawa, M. Yamaguchi, *Polym. J.* **2018**, *50*, 857.
[28] Q. Rong, W. Lei, L. Chen, Y. Yin, J. Zhou, M. Liu, *Angew. Chem., Int. Ed. Engl.* **2017**, *56*, 14159.

[29] D. Zhou, F. Chen, S. Handschuh-Wang, T. Gan, X. Zhou, X. Zhou, *ChemPhysChem* **2019**, *20*, 2139.
[30] Y. Wang, C. Zhu, R. Pfattner, H. Yan, L. Jin, S. Chen, F. Molina-Lopez, F. Lissel, J. Liu, N. I. Rabiah, Z. Chen, J. W. Chung, C. Linder, M. F. Toney, B. Murmann, Z. Bao, *Sci. Adv.* **2017**, *3*, e1602076.
[31] a) Y. Zhuo, S. Xiao, V. Håkonsen, T. Li, F. Wang, J. He, Z. Zhang, *Appl. Mater. Today* **2020**, *19*, 100542; b) X. Zheng, H. Yang, Y. Sun, Y. Zhang, Y. Guo, *Smart Mater. Struct.* **2018**, *27*, 105013.
[32] C. Wang, K. Hu, W. Li, H. Wang, H. Li, Y. Zou, C. Zhao, Z. Li, M. Yu, P. Tan, Z. Li, *ACS Appl. Mater. Interfaces* **2018**, *10*, 34302.
[33] C. Yang, Z. Suo, *Nat. Rev. Mater.* **2018**, *3*, 125.
[34] C. H. Yang, B. Chen, J. J. Lu, J. H. Yang, J. Zhou, Y. M. Chen, Z. Suo, *Extreme Mech. Lett.* **2015**, *3*, 59.